RSC Advances

PAPER

View Article Online
View Journal | View Issue

Cite this: *RSC Adv.*, 2025, **15**, 18310

Core/shell molecularly imprinted nanoparticles: optimized synthesis and application in QCM-D biosensing

Mariacristina Gagliardi* and Marco Cecchini

Molecularly imprinted nanoparticles (MI-NPs) are synthetic receptors with high selectivity and stability, offering advantages for biosensing applications. In this study, we developed and optimized core/shell molecularly imprinted nanoparticles (CS-MI-NPs) tailored for quartz crystal microbalance with dissipation monitoring (QCM-D) sensors. The nanoparticles were synthesized through a controlled sol–gel process, achieving tunable sizes (22–63 nm) and high monomer conversion. Functionalization with amine and vinyl groups facilitated imprinting of a selective shell, enhancing the recognition capabilities of CS-MI-NPs. The optimized system demonstrated significantly improved binding performance, with a specific surface area increase of 260–270% and a target protein retention rate of 34–37%, compared to 6–12% in non-imprinted controls. Langmuir modeling confirmed high affinity and selective binding sites, while QCM-D measurements validated efficient immobilization, low nonspecific interactions, and a detection limit of 2.8 nM for streptavidin. Additionally, CS-MI-NPs selectively recognized tannins in complex mixtures, distinguishing between proanthocyanidins, ellagic, and gallic tannins, with detection levels comparable to biologically derived probes. These results highlight CS-MI-NPs as a versatile and high-performance platform for nanostructured biosensors, with potential applications in biomedical diagnostics, environmental monitoring, and food analysis.

Received 2nd April 2025
Accepted 24th May 2025

DOI: 10.1039/d5ra02297e

rsc.li/rsc-advances

1 Introduction

Molecular imprinting (MI) is a powerful and versatile synthetic strategy for designing polymers with molecular recognition capabilities. By polymerizing functional monomers in the presence of a template molecule, it is possible to create binding sites that are spatially and chemically complementary to the target. Upon template removal, the resulting cavities can selectively rebind the target with high affinity and specificity, mimicking the function of natural receptors such as antibodies or enzymes.[1–3] This approach is particularly appealing in applications where the need for stability, robustness, and long-term storage often limits the use of biological recognition elements. Natural receptors are subject to degradation, require controlled storage conditions (*e.g.*, refrigeration), and often suffer from limited shelf life and batch-to-batch variability. In contrast, molecularly imprinted polymers (MIPs) exhibit exceptional thermal and chemical stability, are compatible with a wide range of solvents and pH conditions, are reusable and can be stored at room temperature without significant loss of performance. These features make MIPs particularly suited for field-deployable, durable, and cost-effective sensing platforms.

NEST, Istituto Nanoscienze-CNR, Scuola Normale Superiore, Piazza San Silvestro, Pisa, I-56127, Italy. E-mail: mariacristina.gagliardi@cnr.it

Molecularly imprinted nanoparticles (MI-NPs) can be tailored to a wide range of targets by rational design of monomer-template interactions and polymerization conditions.[4] Over the years, MI-NPs have attracted increasing interest in biosensing[5,6] due to their specificity in recognizing proteins,[7–9] nucleic acids,[10] and small organic compounds.[11,12]

Originally developed for small molecule recognition, molecular imprinting has been adapted to address the challenges associated with larger biomolecules, such as conformational flexibility, complex surface topography, and aqueous solubility. Strategies such as epitope imprinting have been introduced to overcome these limitations.[13] Surface imprinting is another key approach that allows for the creation of a thin imprinted shell around a solid core, thus enhancing accessibility of the recognition sites and improving both binding kinetics and sensitivity.[14–17]

Surface-imprinted core/shell nanoparticles (CS-MI-NPs) are particularly advantageous for imprinting large biomolecules such as proteins, which present considerable challenges due to their size, structural complexity, and conformational dynamics.[18] CS-MI-NPs offer precise control over particle size and surface chemistry, reduced mass transport limitations, and enhanced performance in aqueous environments. The synthesis of a MI system requires careful optimization of various factors, such as functional monomers,[19] cross-linkers,[20]

and polymerization conditions.[21,22] As a rule, operative conditions are critical for achieving high affinity and specificity for the target molecule.[23] Surface imprinting of CS-MI-NPs also enables precise control over nanoparticle size and shell thickness, thereby improving binding efficiency and minimizing nonspecific adsorption.[24]

After synthesis, CS-MI-NPs can be integrated into biosensing platforms. Quartz crystal microbalance with dissipation monitoring (QCM-D) is a powerful tool for real-time detection of substances.[25–28] Functionalizing QCM-D sensors with MI-NPs allows for the creation of highly selective biosensors for protein detection. The functionalization of QCM-D sensors with MI-NPs has already been demonstrated for protein detection.[29] Recent studies have explored the application of MI-functionalized QCM sensors for detecting various proteins, significantly improving sensitivity and selectivity (*e.g.*[30–32]). In this context, the use of CS-MI-NPs enables the design of stable and selective biosensors for complex biological or environmental targets, while maintaining the reproducibility and scalability required for practical applications.

In addition to proteins, we selected tannins as a second class of target analytes to demonstrate the versatility of the approach across chemically and structurally distinct molecules. Tannins are complex polyphenolic compounds with broad molecular weight distributions, diverse conformations, and a high tendency to aggregate in aqueous media. They are relevant in several fields, including food science, oenology, pharmaceuticals, and environmental monitoring, where their detection and discrimination (*e.g.*, between gallotannins, ellagitannins, and proanthocyanidins) is often required in complex mixtures. The use of MI allows the development of robust and selective recognition elements for such challenging analytes, overcoming the limitations of conventional biosensors based on biological affinity elements. Including tannins in our study enabled us to assess the performance of CS-MI-NPs in conditions of high matrix complexity and structural heterogeneity, thus highlighting their applicability beyond classical protein detection.

In this study, we optimized a surface-imprinted core/shell nanoparticle system against streptavidin (CS-sMI-NPs), aiming to develop a versatile, high-performance sensing platform. As the impact of core size, surface functionalization, monomer composition and concentration, and shell thickness was systematically investigated to maximize recognition efficiency. As a demonstration of applicability, synthesized nanoparticles were integrated in QCM-D sensors and tested for the selective detection of proteins and polyphenolic compounds in complex matrices. Additionally, we tested the same system imprinted against tannins (CS-tMI-NPs), which are large molecules with distinct conformations and compositions compared to streptavidin. Specifically, we conducted a case study by imprinting our nanoparticles with proanthocyanidin tannins and testing them against complex samples containing both proanthocyanidins and ellagitannins. Our findings demonstrate the potential of CS-MI-NPs as effective probes for bulk acoustic waves sensors functionalization.

2 Materials and methods

2.1 Materials

Unless specifically stated otherwise, all reagents were purchased from Sigma-Aldrich. Tetraethyl orthosilicate (TEOS, molecular weight 208.33 g mol^{-1}, specific gravity 0.93 g mL^{-1}, purity > 99%), 3-(trimethoxysilyl)propyl methacrylate (TMPMA, M_w 248.35 g mol^{-1}, specific gravity 1.05 g mL^{-1}, purity 98%), and (3-aminopropyl)triethoxysilane (APTES, M_w 221.37 g mol^{-1}, specific gravity 0.95 g mL^{-1}, purity 99%) served as the primary reagents for core synthesis and subsequent reactive functionalization. Trimethylolpropane trimethacrylate (TRIM, M_w 338.40 g mol^{-1}, specific gravity 1.06 g mL^{-1}, technical grade), 2-hydroxyethyl methacrylate (2-HEMA, M_w 1130.14 g mol^{-1}, specific gravity 1.07 g mL^{-1}, purity > 99%), 2-(dimethylamino)ethyl acrylate (DMAEA, M_w 143.18 g mol^{-1}, specific gravity 0.94 g mL^{-1}, purity 98%), methyl methacrylate (MMA, M_w 100.12 g mol^{-1}, specific gravity 0.94 g mL^{-1}, purity 99%) and 2,2′-azobis(2-methylpropionitrile) (AIBN, M_w 164.21 g mol^{-1}, purity 98%) were used for the synthesis of the imprinted shell. Methylene blue (MB, M_w 319.85 g mol^{-1}, purity > 97%) was used for specific surface tests. Streptavidin (STREP, IBA Lifesciences, 53 kDa, purity > 95%) and bovine serum albumin (BSA, 66 kDa, purity > 96%) were used as proteins in syntheses, rebinding tests, isotherm tests, and QCM-D experiments. Poly(ethylene glycol) 2-mercaptoethyl ether acetic acid (HS–PEG–COOH, NanoCS, 2 kDa), dithiothreitol (DTT, M_w 154.25 g mol^{-1}, purity > 98%), *N*-(3-dimethylaminopropyl)-*N*′-ethylcarbodiimide (EDCl, M_w 191.70 g mol^{-1}, commercial grade), and *N*-hydroxysuccinimide (NHS, M_w 115.09 g mol^{-1}, purity > 98%) were used for adlayer formation and as coupling agents. For the case study, three commercial oenological additives (Laffort, Italy), TANIN VR GRAPE® (TVRG, proanthocyanidin tannins extracted from grapes), TANIN VR SUPRA® (TVRS, proanthocyanidin and ellagitannins), and TANIN GAL-ALCOOL® (TG, gallic tannins) were used for synthesis and QCM-D tests. Absolute ethanol (EtOH, HPLC purity), ammonium hydroxide (NH_4OH, ACS purity, 32% v/v), hydrogen peroxide (H_2O_2, ACS purity, 35% v/v), Milli-Q water, phosphate buffered saline solution (PBS, 140 mM NaCl, 10 mM phosphate buffer, 3 mM KCl, pH 7.4 at 25 °C), hydrochloric acid (HCl, ACS purity, 36% in water), sodium dodecyl sulfate (SDS, molecular biology purity, 20% solution in water), acetic acid (CH_3COOH, glacial, ACS purity degree), and sodium bicarbonate solution ($NaHCO_3$, ACS purity) were used as solvents in syntheses and all tests. Monomers, proteins, and the radical initiator were used as purchased, while solvents were filtered before use.

2.2 Nanoparticle characterization

Photon Correlation Spectroscopy (PCS) was used to measure nanoparticle size, polydispersity index (PDI), and average photon count (kcps). The ζ-potential was also measured using the same apparatus (Zetasizer, Malvern Panalytical, Malvern, UK).

Nanoparticle size was determined by diluting suspensions (~0.1 mg mL^{-1}) in water, placing 50 μL in a quartz cuvette, and measuring. Any protocol modifications are detailed in the text. Raw data were processed with Excel to extract peak mode, full width at half maximum (FWHM), and PDI, fitting a skewed bell-shaped function. Samples were analyzed in triplicate. Additionally, kcps was tracked as an indicator of sample concentration.[33] For ζ-potential, diluted samples were placed in a disposable folded capillary cell and directly analyzed by the software.

UV-Vis spectroscopy (JASCO V550, JASCO Europe) was used to study complex formation, Langmuir isotherms, rebinding tests, and to estimate the specific surface area. Experimental details for sample preparation are provided in the text.

2.3 Synthetic procedures

2.3.1 Nanoparticle core. The nanoparticle core was synthesized using the Stöber method.[34] Reaction parameters were optimized through a pilot synthesis, where 70 mL of EtOH, 1.4 mL of NH_4OH, and 1.0 mL of water were added to a round-bottom reactor. Separately, 4.0 mL of TEOS (18 mmol) diluted in 35 mL of EtOH was added under stirring at room temperature. Aliquots (50 μL) were withdrawn at fixed intervals, diluted in 950 μL of water to halt the reaction, and measured for size and kcps. Sampling continued until parameters plateaued, identifying 24 h as the optimal reaction time for high monomer conversion and stable particle size.

Using the same experimental protocol, three formulations were tested (Table 1) to assess the impact of TEOS concentration on size: S1 (0.20 mM), S2 (0.16 mM), and S3 (0.12 mM). Products were dialyzed for 24 h in EtOH, then stored in sealed vials at room temperature. All syntheses were performed in triplicate.

2.3.2 Reactive functionalization of the core nanoparticles. The core surface was functionalized with amine and vinyl groups using APTES and TMPMA. APTES facilitated interactions with template molecules through amine groups, while TMPMA contributed vinyl groups for shell–core anchoring. The optimal APTES/TMPMA molar ratio and monomer concentration were determined through screening. 50 mg of Stöber nanoparticles were suspended in 10 mL of solution containing 5 mL of EtOH and 5 mL of HCl (1 mM, pH 4) in a sealed vial. APTES and TMPMA were added in concentrations of 1 mM, 2 mM, and 3 mM (monomer-to-nanoparticle ratios: 0.2 μmol mg^{-1}, 0.4 μmol mg^{-1}, and 0.6 μmol mg^{-1}). Molar ratios of 75/25, 50/50, and 25/75 APTES/TMPMA were tested, along with controls using only APTES or only TMPMA. The mixture was stirred for 1 h at room temperature, followed by 24 h dialysis against water (14 kDa MWCO). The final products were stored at room temperature and used within one month.

Table 1 Reactants and solvents used for the core syntheses

Solvent or reagent (mL)	S1	S2	S3
EtOH	6.2	6.3	6.4
NH_4OH	0.13	0.13	0.13
Water	0.09	0.09	0.09
TEOS	0.44	0.36	0.27
EtOH to dissolve TEOS	3.1	3.1	3.2

The best APTES/TMPMA ratio was selected based on nanoparticle size. The formulation was further optimized to find the best balance between monomers and core nanoparticles concentrations. Solvent composition was adjusted to prevent premature monomer hydrolysis, using 1.5 mL water and 4.5 mL EtOH. 30 mg of nanoparticles were used, with monomer concentrations ranging from 0.7 mM to 2.1 mM (0.14 μmol mg^{-1} to 0.36 μmol mg^{-1}). The lower concentration was selected after screening.

2.3.3 Complexes formation. Complex formation plays a critical role in the final performance of MI-NPs, with more stable complexes yielding better performance.[35]

30 mg of functionalized nanoparticles from three batches were diluted in 50 μL of PBS, followed by the addition of 450 μL of STREP solution (200 μg mL^{-1} in PBS). The final STREP-to-nanoparticle ratio was 3 μg mg^{-1}. The mixture was incubated at 75 °C for 5, 10, 20, and 30 min, then centrifuged for 5 min at 13.3 krpm. Supernatants were collected for UV-Vis analysis. Control experiments included functionalized nanoparticles in PBS and a STREP solution without nanoparticles, incubated under the same conditions. The residual STREP concentration was monitored over time to calculate the amount immobilized on the nanoparticles. Data were analyzed upon a calibration curve generated with STREP concentrations ranging from 7.0 μg mL^{-1} to 240 μg mL^{-1} in PBS, with UV-Vis spectra acquired between 220 and 350 nm and absorbance monitored at 280 nm.

Tests were performed in triplicate on three batches of functionalized nanoparticles (9 samples per timepoint). Pellets from samples incubated for 30 min were resuspended in PBS and analyzed by DLS.

2.3.4 Imprinted shell. Functionalized nanoparticles were used to prepare surface-imprinted nanoparticles. Nanoparticles from the S1 synthesis, functionalized with a 50/50 molar ratio of APTES/TMPMA at 0.14 μmol mg^{-1}, were tested with a STREP-to-nanoparticle ratio of 3 μg mg^{-1}.

5 mg of functionalized nanoparticles in water suspension (1 mg mL^{-1}) was added to a mixture of 4 mL EtOH and 1 mL 1% SDS solution (w/v). The mixture was stirred and heated to 75 °C. Once at temperature, a fixed volume of a monomer mixture (2-HEMA, DMAEA, MMA, and TRIM, molar ratio 1 : 1 : 1 : 2) dissolved in EtOH was added. The concentrations in the monomer mixture were 60 mM for 2-HEMA, DMAEA, and MMA, and 120 mM for TRIM. Six different volumes of the monomer mixture were tested, resulting in a monomer-to-nanoparticle ratio ranging from 0.45 μmol mg^{-1} to 13.6 μmol mg^{-1} to study the effect on nanoparticle size. Nanoparticles were washed with an extraction solution (0.1% w/v of SDS, 0.1% v/v in CH_3COOH, $T = 45$ °C, 30 min) then centrifuged (13.3 krpm for 15 min). The pellet was then recovered and washed twice with water.

Among the formulations tested, the monomer-to-nanoparticle ratio of 0.45 μmol mg^{-1} was chosen for subsequent characterizations.

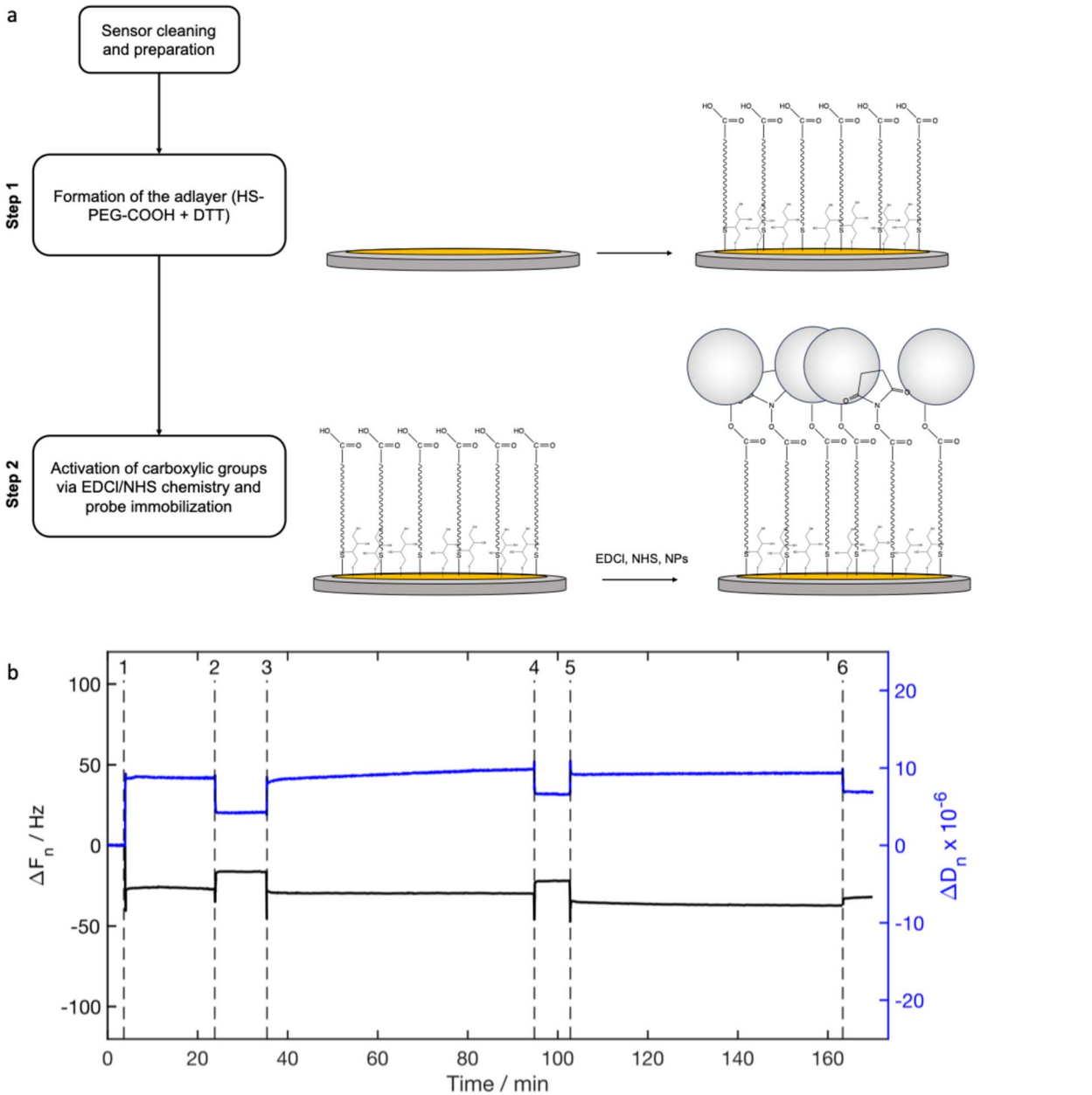

Fig. 1 QCM-D characterization: (a) schematization of the sensor functionalization (not in scale); (b) characteristic traces of the whole experiment (events: (1) injection of the adlayer solution, (2) rinsing with water, (3) injection of the probe solution, (4) rinsing with water, (5) injection of the sample solution, (6) rinsing with water).

2.4 Nanoparticle characteristics and performance

2.4.1 Specific surface. The specific surface area of CS-sMIP-NPs was estimated using the methylene blue (MB) assay.[36] 0.10 mg of nanoparticles were suspended in 50 μL of water and incubated with 150 μL of MB solution in EtOH (10 μg mL^{-1}) for 24 h. After incubation, samples were centrifuged (13.3 krpm for 5 min), and the supernatant was analyzed by UV-Vis spectroscopy. Data were processed using a calibration curve (concentrations from 3.0 μg mL^{-1} to 50.0 μg mL^{-1}), with spectra were acquired between 500 nm and 750 nm, monitoring the absorbance at 658 nm. Samples were tested at varying monomer-to-nanoparticle ratio. Core/shell non-imprinted nanoparticles (NIPs, monomer-to-nanoparticle ratio of 0.40 μg mg^{-1}, size 165 nm ± 68 nm) were synthesized and tested as a control.

The specific surface area (A_s) of the nanoparticles was calculated using eqn (1):

$$A_s = \frac{q_{MB} N_A \phi_{MB}}{M_{MB} m} \quad (1)$$

where q_{MB} is the amount (g) of absorbed MB, N_A is the Avogadro's number (6.022×10^{23} mol^{-1}), ϕ_{MB} is the surface area occupied by a single MB molecule on the adsorbent surface (1.3×10^{-18} m^2), M_{MB} is the molecular weight of MB (319.9 g mol^{-1})

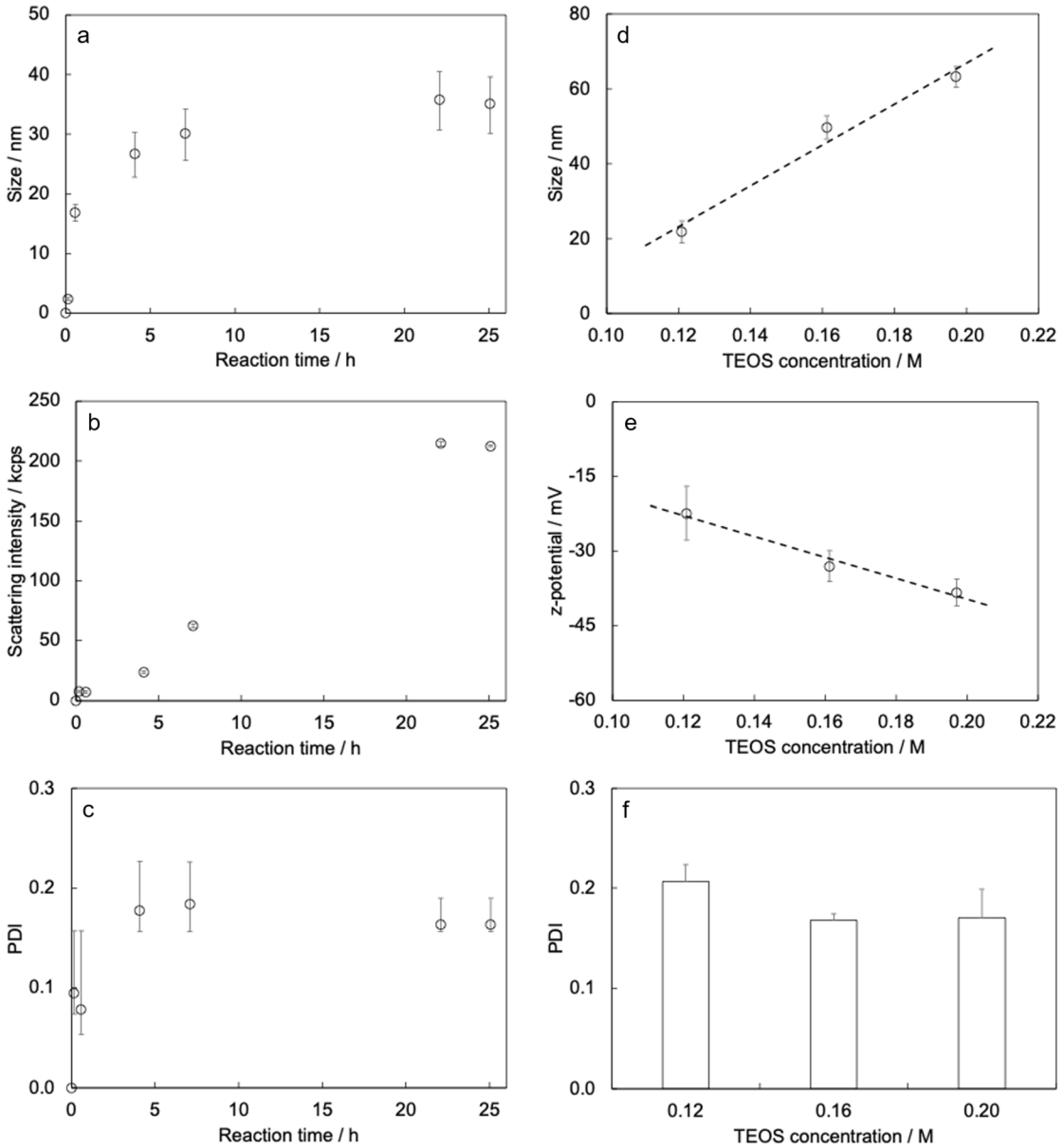

Fig. 2 Preliminary synthesis and core characterization: (a)–(c) size, scattering intensity and PDI respectively, measured during nanoparticle growth, (d)–(f) size, *z*-potential and PDI respectively, measured in the screening syntheses to determine the preferred TEOS concentration. In growth kinetics plots, three samples were withdrawn from the reactive mass and measured, thus reported error bars represent the range max/min.

and m is the mass of nanoparticles (mg). Tests were performed in triplicate.

2.4.2 Rebinding tests and equilibrium isotherms. Rebinding tests were conducted by incubating 5 mg of CS-sMI-NPs in a solution of STREP in PBS (180 μg mL^{-1}). At fixed times (5, 10, 20, 40, and 60 min), samples were centrifuged (13.3 krpm for 5 minutes), and the supernatant was collected and analyzed by UV-Vis spectroscopy. Spectra were acquired as previously described. A calibration curve for STREP was constructed by analyzing solutions with known concentrations in the range of 10 μg mL^{-1} to 500 μg mL^{-1}. Tests were conducted in triplicate.

Equilibrium isotherms were studied to evaluate CS-sMI-NPs, selecting the system with the highest rebinding capacity. For the isotherms, 50 μg of CS-sMI-NPs or NIPs were mixed with 150 μL protein solutions, with concentrations in the range from 100 μg mL^{-1} to 200 μg mL^{-1}, of STREP (target protein) or BSA (negative control) and incubated for 24 h at room temperature. After centrifugation (13.3 krpm for 5 minutes), the supernatants were analyzed by UV-Vis spectroscopy, monitoring absorbance at 280 nm for both proteins. Calibration curves for STREP and BSA were obtained in the range from 6 μg mL^{-1} to 16 μg mL^{-1}. Tests were conducted in triplicate. Experimental data were fitted using the Langmuir model[37] (eqn (2)):

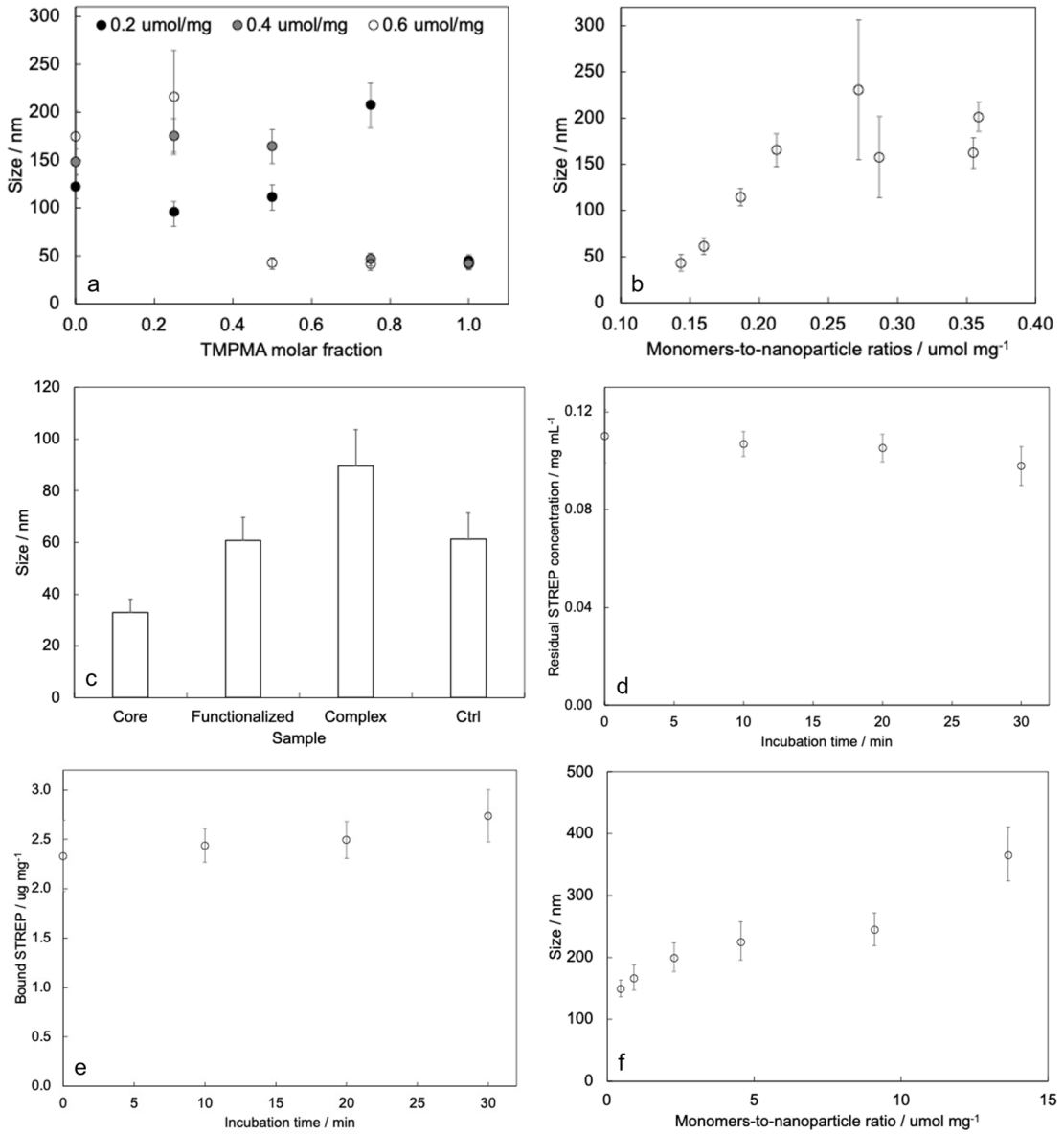

Fig. 3 Measured size of functionalized nanoparticles in different screening tests: (a) effect of APTES/TMPMA molar ratios and (b) effect of the overall monomers-to-nanoparticle concentration. Data are the mean value of mode values calculated for three syntheses for each point, error bars represent the SE. The starting size of bare core nanoparticles was 35 nm ± 5 nm. Study of the STREP/nanoparticles complex formation and characterization of CS-sMI-NPs: (c) size of tested nanoparticles (core: bare Stöber from S1 synthesis; functionalized: core nanoparticles functionalized with a APTES/TMPMA ratio of 50/50 and monomer-to-nanoparticle concentration of 0.16 μmol mg^{-1}; complex: STREP/nanoparticle complex after 30 min of incubation in the protein solution; Ctrl: functionalized nanoparticles incubated in PBS), UV-Vis measurements of (d) supernatant collected from the incubation solution; (e) differential concentration normalized over the amount of functionalized nanoparticles; (f) size of CS-sMI-NPs by varying the monomers concentration in the reaction.

$$Q_e = Q_m \frac{K_L c_e}{1 + K_L c_e} \quad (2)$$

where Q_e is the equilibrium adsorption capacity (mg mg^{-1}), Q_m is the maximum adsorption capacity (mg mg^{-1}), K_L is the Langmuir constant, indicating the affinity between adsorbent and adsorbate (mL mg^{-1}), and c_e is the equilibrium concentration in the incubation solution (mg mL^{-1}).

Additional characteristic parameters were calculated to quantify the system performance, including the Imprinting Factor (IF, eqn (3)) and the Relative Affinity (RA, eqn (4)):

$$IF = \frac{Q_{m,MIP}}{Q_{m,Ctrl}} \quad (3)$$

$$RA = \frac{K_{L,MIP}}{K_{L,Ctrl}} \quad (4)$$

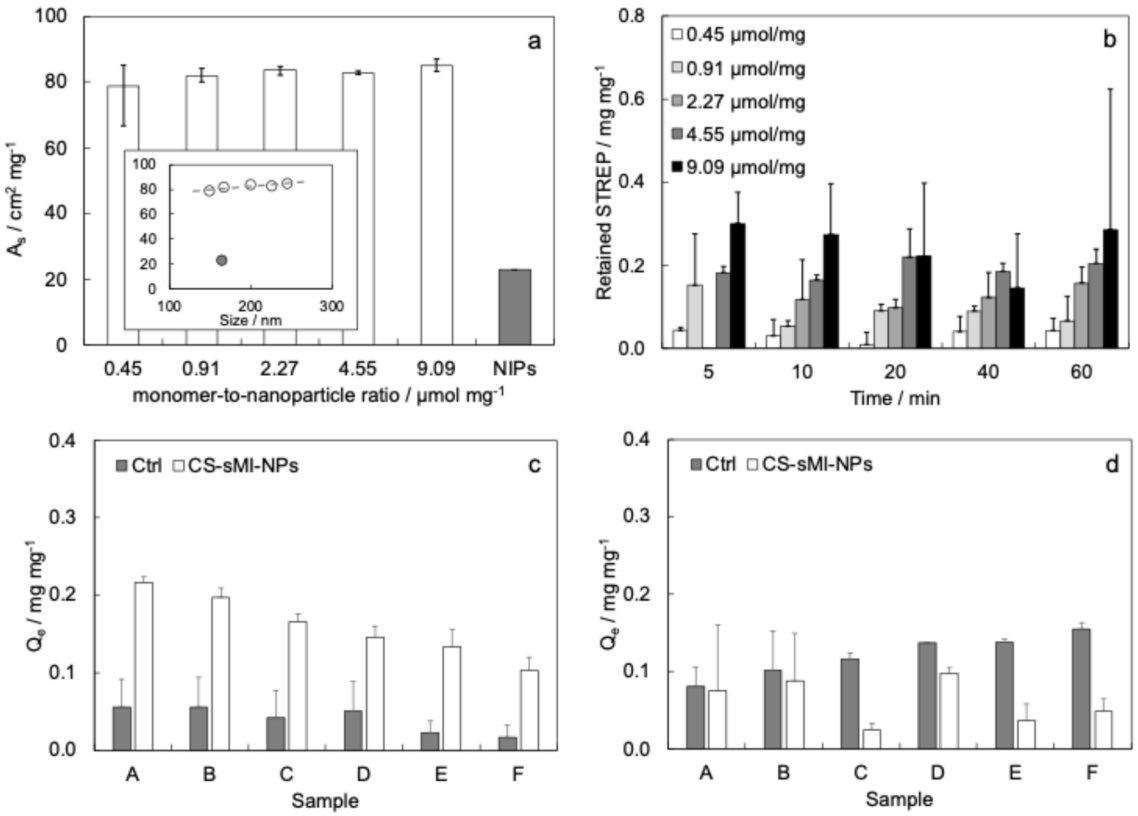

Fig. 4 UV-Vis characterization of CS-sMI-NPs: (a) estimation of the specific surface A_s (eqn (1)) *via* methyl blue adsorption test as a function of the monomer-to nanoparticle ratio and the nanoparticle size (inset) compared to the value obtained for NIPs (gray), (b) amount of retained STREP normalized over the amount of nanoparticles as a function of the time in rebinding tests by varying the monomer-to-nanoparticle ratio; amount of retained (c) STREP and (d) BSA over the amount of nanoparticles at the equilibrium (24 h) measured after incubation with protein solutions with decreasing protein concentrations.

Table 2 Computed parameters from the Langmuir modelling

	Parameter	Specific (STREP)	Nonspecific (BSA)
Eqn (3)	$IF = \frac{Q_{m,CS\text{-}sMI\text{-}NPs}}{Q_{m,Ctrl}}$	2.65	—
Eqn (4)	$RA = \frac{K_{L,CS\text{-}sMI\text{-}NPs}}{K_{L,Ctrl}}$	1.44	—

where Q_m and K_L were previously described. For the Langmuir parameter calculations, experimental data were processed using MATLAB 2023b (MathWorks, Natick, US).

2.5 QCM-D experiments

The QCM-D (E4 model, Q-Sense AB, Sweden) experiments were conducted using AT-cut quartz crystals with gold electrodes. The sensors (Biolin Scientific, Västra Frölunda, Sweden) had a fundamental resonance frequency (f_0) of 5 MHz, an overall diameter of 14 mm, and a gold-coated active area with a diameter of 10 mm. Sensors were mounted in microfluidic chambers, and measurements were performed in stagnant mode at 25 °C.

Before use, sensors were cleaned with oxygen plasma (Femto, Diener Electronic, Ebhausen, Germany) for 2 min at a power of 100 W, soaked in a 5 : 1 : 1 v/v/v solution of water, NH_4OH, and H_2O_2 at 75 °C for 15 min, rinsed with water and isopropanol, dried under dry N_2, and treated again with oxygen plasma for 2 min.

To modify the gold surface, an HS–PEG–COOH adlayer was formed *via* thiol–gold chemistry. Sensors, mounted in QCM-D chambers and pre-rinsed with water, were treated with an adlayer solution of HS–PEG–COOH (2 mg mL^{-1}) and DTT (5 times the molar concentration of HS–PEG–COOH) in $NaHCO_3$ (0.1 M) for 15 min, followed by a water rinse (5 min). This process exposed carboxylic functionalities for probe immobilization.

For nanoparticle immobilization, a solution containing nanoparticles (2 mg mL^{-1}), EDCl, and NHS (50 mM each) in water was injected into the chambers. After 60 min, the sensors were rinsed with water (5 min). Fig. 1a shows the functionalization process, while Fig. 1b reports typical QCM-D traces.

After functionalization, sample solutions containing the protein of interest in PBS (STREP or BSA, 0.15 mg mL^{-1}) were injected and incubated for 60 min. Finally, the sensors were rinsed with water (5 min).

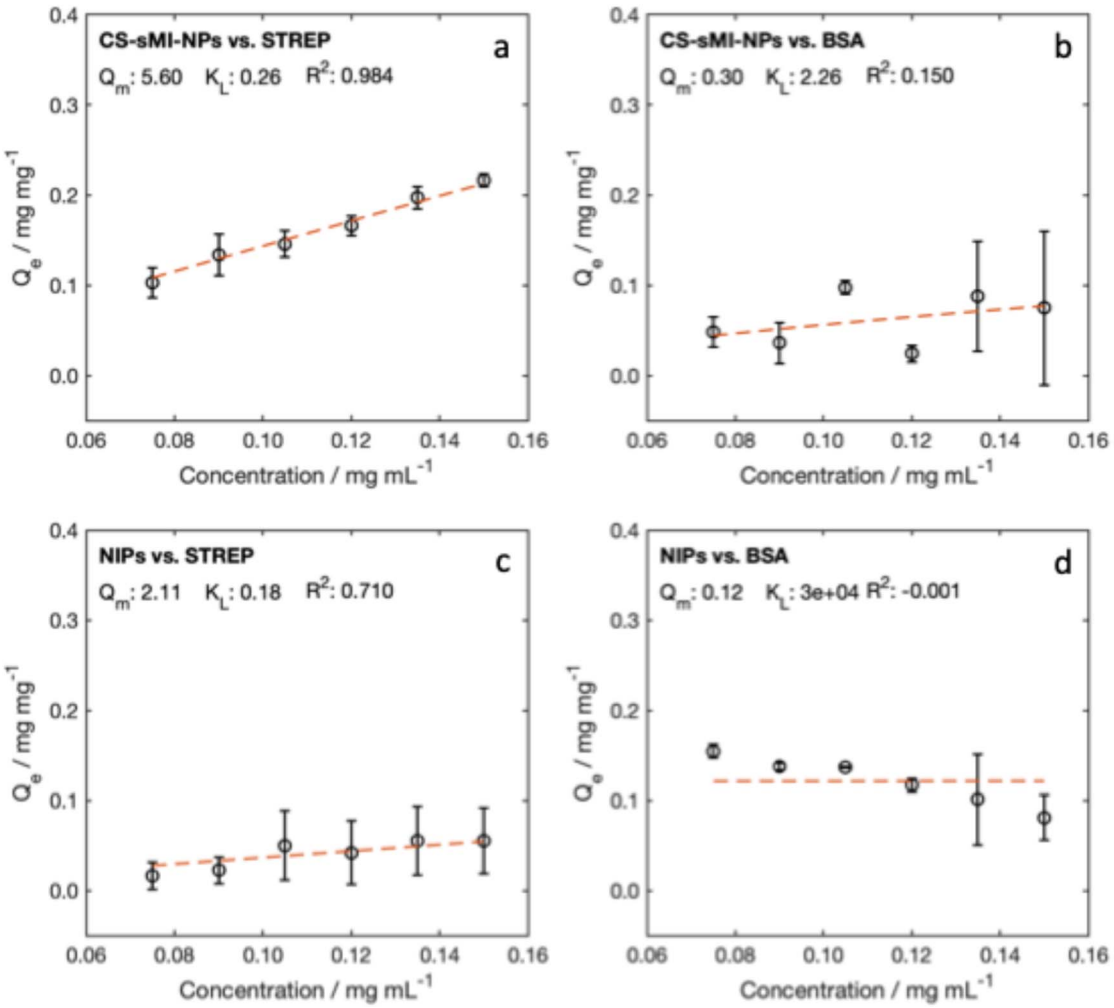

Fig. 5 Isotherm adsorption and Langmuir model: experimental data of Q_e *vs.* protein concentration (○), Langmuir fitting (--), and calculated parameters.

2.6 Case study

The CS-MI-NPs system was tested for recognizing oenological tannins. Core/shell tannin-imprinted nanoparticles (CS-tMI-NPs) were prepared and tested using the same procedures as for CS-sMI-NPs but changing the template molecule. For CS-tMI-NPs, the mixture TVRG was used during synthesis. QCM-D tests were performed using TVRG (specific recognition), TVRS (competitive recognition), and TG (nonspecific adsorption) as analytes. The system used nanoparticles from S1 as the core, functionalized with 50/50 APTES/TMPMA mixture at 0.14 μmol mg^{-1}, a template-to-nanoparticle ratio of 3 μg mg^{-1}, and a monomer-to-nanoparticle ratio of 0.45 μmol mg^{-1}. QCM-D sample concentration was 0.2 mg mL^{-1}.

2.7 Data analysis

In PCS and ζ-potential experiments, data are reported as the mean mode calculated from replicates. For technical replicates, results are expressed as the mean mode ± FWHM, while for independent experiments, data are reported as the mean mode ± SE. In nanoparticle growth kinetics, a single synthesis was monitored, with five samples taken per timepoint; data are the mean of these measurements, with error bars representing the data range.

In UV-Vis measurements, data are reported as mean ± SD for technical replicates, or mean ± SE for independent experiments.

For QCM-D experiments, the apparatus recorded the resonance frequency shift (Δf) and energy dissipation (ΔD) for up to seven odd overtones, while only the 3rd to the 11th overtones were used for data analysis. The values of $\Delta F_n = \Delta f_n/n$ are reported. ΔF_n and ΔD_n were calculated as the difference between the baseline acquired at the start of each measurement step and the post-rinse signals. At least three experiments were performed for each condition, with ΔF_n (Hz), ΔD_n (dimensionless), and molecular density (molecules per cm^2) continuously recorded. Results are presented as the mean of replicates (N), with error bars indicating the SE. The fundamental frequency (ΔF_0) was excluded due to environmental noise sensitivity.[38]

The adhered sensor mass was evaluated using the Sauerbrey model (eqn (5)).[39] The Sauerbrey equation is as follows:

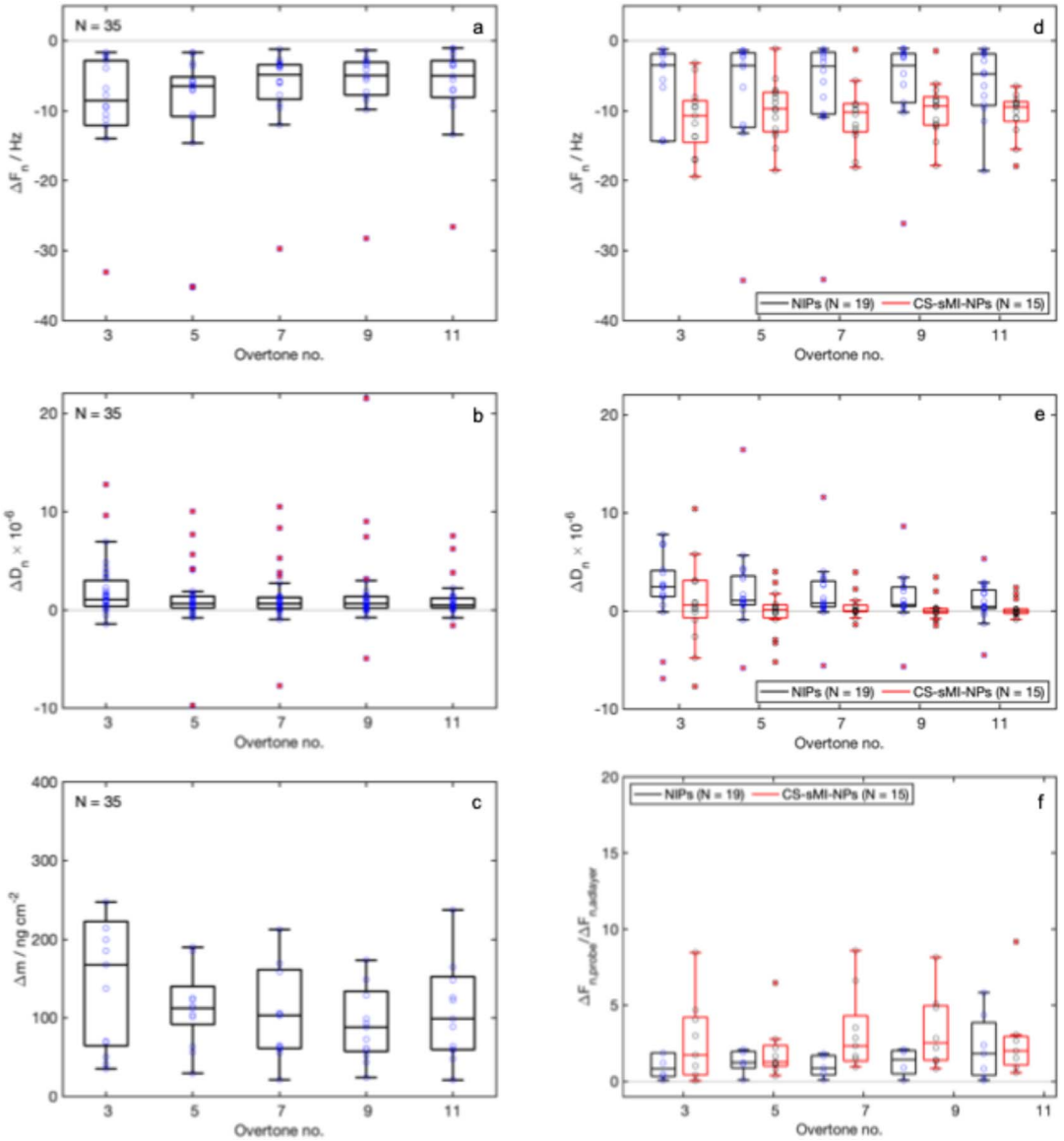

Fig. 6 QCM-D results related to sensor functionalization: (a) ΔF_n and (b) ΔD_n measured after the formation of the adlayer, (c) Δm calculated for the adlayer by using the Sauerbrey equation (eqn (5)), (d) ΔF_n and (e) ΔD_n measured after the immobilization of the nanoparticle probes, (f) normalized ΔF_n measured after the probe immobilization over the ΔF_n measured after the adlayer immobilization. *N* indicates the number of tested sensors.

$$\Delta m = -C \cdot \Delta F_n \quad (5)$$

In this equation, Δm is the variation in sensor mass (ng cm^{-2}), C is the mass sensitivity constant (17.7 ng cm^{-2} Hz^{-1} for quartz crystals with $f_0 = 5$ MHz), n is the overtone number.

In this work, the Sauerbrey model was applied if at least one of the following three criteria was met: (1) minimal dependence of ΔF_n on n, (2) ΔD_n values below 2×10^{-6}, (3) $\Delta D_n/(-\Delta F_n) \ll 4 \times 10^{-7}$ Hz.[40,41]

The molecular density was calculated form the areal mass as follows (eqn (6)):

$$\text{Molecular density} = \frac{\Delta m}{M_w} \times N_A \quad (6)$$

In this equation, M_w is the molecular weight of the considered compound (g mol^{-1}).

3 Results

3.1 Dimensional characterization

3.1.1 Preliminary analysis of nanoparticle core size and growth kinetics. Nanoparticle growth kinetics was monitored to determine the optimal reaction time for achieving high monomer conversion, stable nanoparticle size, and sufficient concentration. Both size and scattering intensity reached a plateau after 22 h. The growth trend followed a power-law behavior (Fig. 2a), indicating rapid expansion of the dominant nanoparticle fraction. Conversely, the kcps trend (Fig. 2b)

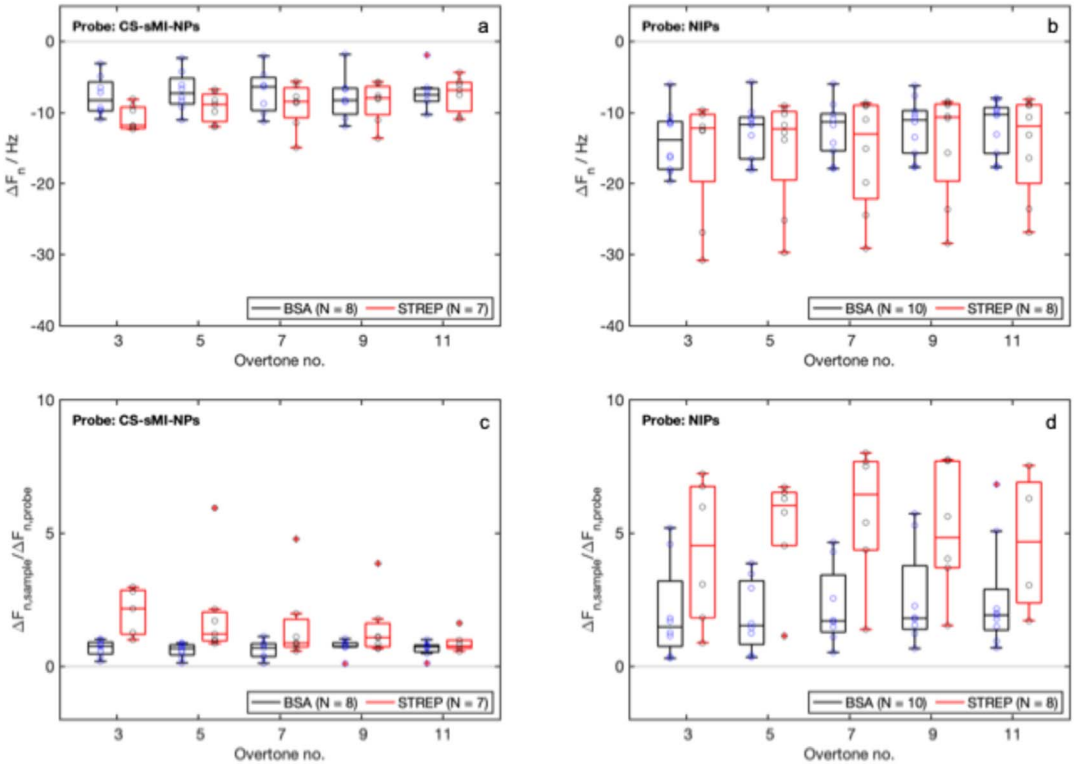

Fig. 7 QCM-D experiments, detection of the samples: (a) and (b) ΔF_n measured for CS-sMI-NPs and NIPs after the detection of the reference protein (STREP, specific signal) and the control protein (BSA, nonspecific signal), (c) and (d) normalized ΔF_n in respect to the values of ΔF_n measured for probe immobilization for CS-sMI-NPs and NIPs. *N* indicates the number of tested sensors.

exhibited a sigmoid pattern, suggesting limited nanoparticle population at early times. Polydispersity index (PDI) values ranged from 0.10 to 0.22, with a final PDI of 0.18, suitable for the intended application. Consequently, we selected a reaction time of 24 h.

The study of TEOS concentration on nanoparticle size indicated that increasing concentrations resulted in larger Stöber nanoparticles (Fig. 2d): 22 ± 3 nm (0.12 M), 50 ± 3 nm (0.16 M), and 63 ± 3 nm (0.20 M). This trend appeared linear, enabling precise size tuning within this range. Conversely, ζ-potential decreased linearly with increasing TEOS concentration (Fig. 2e): −22.4 mV ± 5.4 mV (0.12 M), −33.0 mV ± 3.2 mV (0.16 M), and −38.3 mV ± 2.7 mV (0.20 M). The PDI (Fig. 2f) showed minimal variation across concentrations, with values of 0.21 ± 0.02 (0.12 M), 0.17 ± 0.03 (0.16 M), and 0.17 ± 0.01 (0.20 M). These results indicate high monomer conversion and homogeneous nanoparticle growth.

Based on this optimization, the reaction condition designated as S1 (see Table 1) was chosen for subsequent experiments.

3.1.2 Reactive functionalization. The silica surface of core nanoparticles was functionalized *via* silanization using APTES and TMPMA. In the initial screening, we tested three APTES/TMPMA molar ratios and three monomer-to-nanoparticle ratios to assess their effect on nanoparticle size. Higher APTES/TMPMA ratios led to larger nanoparticles (Fig. 3a). At 50/50 and 25/75 ratios, TMPMA concentration affected the size, with functionalized nanoparticles reaching 43 nm ± 7 nm at a 50/50 ratio and a monomer-to-nanoparticle ratio of 0.60 μmol mg^{-1}, like TMPMA-only controls. At a 25/75 ratio and higher monomer concentrations (0.40 and 0.60 μmol mg^{-1}), sizes were 42 nm ± 6 nm and 47 nm ± 7 nm, respectively. In control conditions with APTES alone, nanoparticle size increased with higher monomer concentrations, reaching a size difference of about 30 nm, while TMPMA-only functionalization resulted in sizes around 45 nm ± 7 nm. A higher APTES/TMPMA ratio (75/25) also led to larger sizes but without proportionality. These results indicated that TMPMA inhibited APTES functionalization at higher TMPMA-to-nanoparticle ratios. Therefore, we chose a 50/50 APTES/TMPMA ratio for further analysis.

In the additional study, after setting the APTES/TMPMA ratio, monomer-to-nanoparticle concentrations ranged from 0.14 μmol mg^{-1} to 0.36 μmol mg^{-1} (Fig. 3b). Functionalization with 0.14 μmol mg^{-1} yielded nanoparticles of 43 nm ± 9 nm, which was excluded. Higher concentrations resulted in sizes ranging from 60 nm to 200 nm. The formulation with 0.16 μmol mg^{-1} produced nanoparticles of 61 nm ± 9 nm, which was selected for further study.

3.1.3 Complexes formation. The formation of STREP/functionalized nanoparticle complexes was investigated to optimize the performance of the final imprinted particles. In this experiment, we used S1 as core nanoparticles, functionalized with an APTES/TMPMA molar ratio of 50/50 and a starting monomer-to-nanoparticle concentration of 0.16 μmol mg^{-1}.

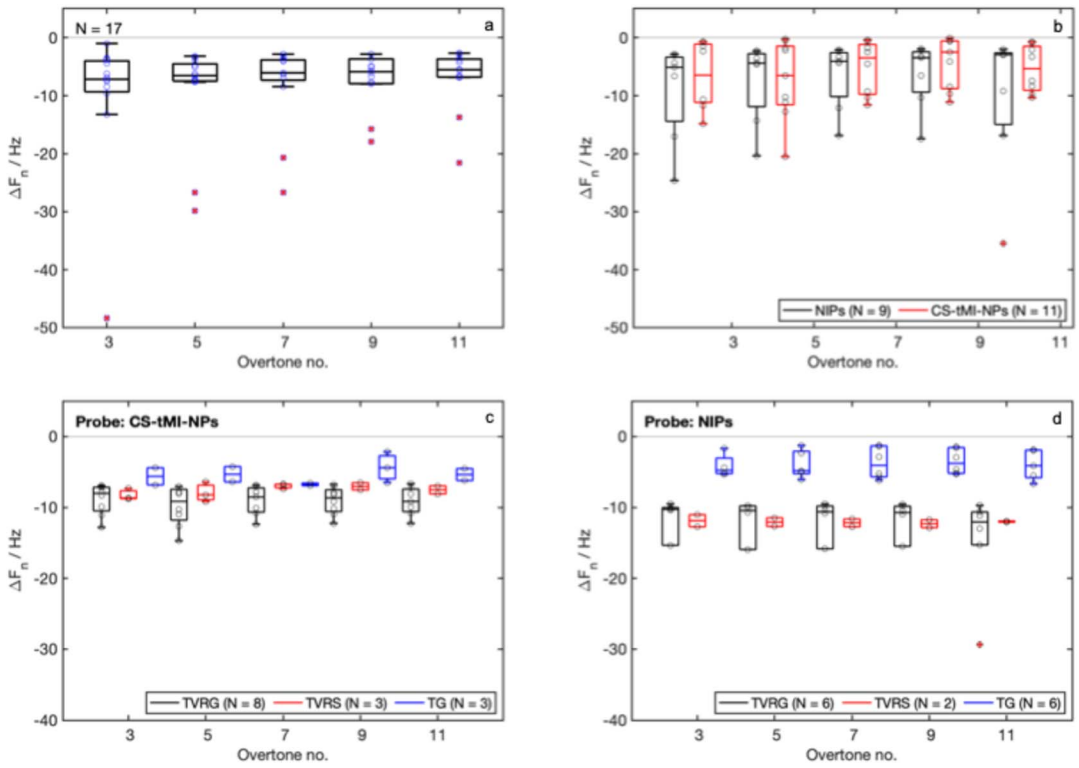

Fig. 8 QCM-D results related to the case study: (a) ΔF_n measured after the adlayer formation; (b) ΔF_n measured after the immobilization of the CS-tMI-NPs and NIPs; (c) and (d) ΔF_n measured after the detection of three samples, TVRG (specific), TVRS (competitive) and TG (nonspecific) for CS-tMI-NPs and NIPs. *N* indicates the number of tested sensors.

The size of the complex STREP/nanoparticles (Fig. 3c) increased to 90 nm ± 14 nm, reflecting a 50% increase compared to the size of the functionalized nanoparticles. NIPs incubated with PBS did not show any change in size (61 nm ± 10 nm).

The concentration of STREP in the incubation solution decreased over time in samples containing the functionalized nanoparticles (Fig. 3d). In contrast, no decrease was observed in the control sample containing only STREP, confirming that high temperature and strong centrifugation did not affect the stability of the protein solution. The residual STREP concentration at the first checkpoint was 61% ± 6% in respect to the starting STREP amount and decreased to 54% ± 4% by the end of the test.

The amount of STREP retained by complexes normalized to the amount of nanoparticles in the samples (Fig. 3e) indicated that, at the end of the incubation, the STREP-to-nanoparticle ratio was approximately 2.7 μg mg^{-1} ± 0.3 μg mg^{-1}.

3.1.4 Surface-imprinted nanoparticle size. The size of the surface-imprinted nanoparticles (CS-sMI-NPs) was influenced by the monomer concentration in the reaction (Fig. 3f). The increase in size was nearly linear across the analyzed range of monomer concentrations. The formation of the imprinted shell significantly contributed to the size of the functionalized nanoparticles, even at lower monomer concentrations. The measured sizes ranged from 150 nm ± 14 nm to 365 nm ± 45 nm.

3.1.5 Specific surface area, rebinding tests, Langmuir isotherms and modelling. Experimental data (Fig. 4a) reveal a mild increase in the specific surface area (A_s) of CS-sMI-NPs with higher monomer concentrations during synthesis. As the monomer concentration increases from 0.45 μmol mL^{-1} to 9.09 μmol mL^{-1}, A_s linearly ranged from approximately 79 cm^2 mg^{-1} to 85 cm^2 mg^{-1} (Fig. 4a-inset). NIPs displayed a much lower A_s of about 23 cm^2 mg^{-1}. This result highlights that molecular imprinting created effective binding cavities, increasing the exposed surface area by 260–270%.

The rebinding tests (Fig. 4b) revealed a strong dependency of STREP binding capacity on nanoparticle synthesis and incubation time. The binding peaked at 40 minutes for the lowest monomer concentration before stabilizing. At the monomer concentration of 0.91 μmol mL^{-1}, binding efficiency improved, with the highest value recorded at the earliest time point (0.30 mg mg^{-1}) followed by minor fluctuations. Intermediate monomer concentrations (2.27, 4.55, and 9.09 μmol mL^{-1}) produced moderate binding levels.

Isotherm tests confirmed the dependence of STREP binding on protein concentration and highlighted significant differences between CS-sMI-NPs and NIPs. While NIPs exhibited lower binding and higher variability, CS-sMI-NPs retained 34% to 37% of STREP, compared to only 6% to 12% for Ctrl. Tests with BSA revealed nonspecific adsorption for both nanoparticle types, with no trends related to protein concentration or nanoparticle formulation.

Equilibrium isotherms further emphasized the superior performance of CS-sMI-NPs. The maximum adsorption capacity (Q_m) for STREP was 5.60 mg mg^{-1} in CS-sMI-NPs, significantly higher than 2.11 mg mg^{-1} for Ctrl. However, the Langmuir constant (K_L), indicative of binding affinity, was relatively low for STREP (0.26 mL mg^{-1}), suggesting limited interaction strength despite the high density of binding sites. For BSA, a higher K_L (2.26 mL mg^{-1}) combined with a lower Q_m (0.30 mg mg^{-1}) reflected nonspecific interactions likely driven by the affinity of BSA toward the polymer matrix.[42]

The imprinting factor (IF) and the relative adsorption affinity (RA) for STREP resulted 2.65 and 1.44 respectively (Table 2). These parameters were not calculated for BSA due to poor fitting. The CS-sMI-NPs retained approximately 36% of STREP, independent of protein concentration, while BSA retention was around 14%. In NIPs, STREP adsorption was limited to 8%, and BSA exhibited a linear decrease from 51% to 13%, indicating surface saturation from nonspecific binding (Fig. 5).

3.2 QCM-D experiments

3.2.1 Sensor functionalization. The ΔF_n values measured in the adlayer formation (Fig. 6a) were all negative, confirming that the immobilization occurred correctly. Statistical analysis on the obtained data revealed no statistically significant differences across the harmonic numbers (Shapiro–Wilk, p-value > 0.05, one-way ANOVA p-value = 0.30). The values of ΔD_n were small and close to zero (Fig. 6b). The lack of dependency of ΔF_n on n and the low values of ΔD_n allowed excluding significant effects due to the adlayer viscoelasticity, allowed the application of the Sauerbrey equation to calculate the mass adhered to the sensor and the molecular density (Fig. 6c). The mean value of adhered mass over all the overtones was 114 ng cm^{-2} ± 31 ng cm^{-2}, corresponding to 34 × 10^{12} molecules per cm^2 ± 9.4 × 10^{12} molecules per cm^2. Results are in line with our previous experiments.[43]

The ΔF_n values measured for the immobilization of both probes were negative (Fig. 6d), indicating successful immobilization. The measured ΔF_n values for CS-sMI-NPs and NIPs did not show a dependency on n (Shapiro–Wilk, p-value > 0.05 for both groups, one-way ANOVA p-value = 0.99 and 0.37 respectively). The measured ΔD_n values after probe immobilization were close to zero in all cases (Fig. 6e). The lack of dependency of ΔF_n on n and the low values of ΔD_n allowed excluding significant effects due to the viscoelasticity of the whole functionalization.

The ΔF_n signals obtained for the probes were normalized with respect to the ΔF_n signals obtained for the adlayer (Fig. 6f). The values obtained for CS-sMI-NPs were slightly higher compared to those obtained for NIPs, but with no statistically significant differences (t-test).

3.2.2 Sample detection. The detection of STREP and BSA with both CS-sMI-NPs (Fig. 7a) and NIPs (Fig. 7b) confirmed the improved performance of imprinted nanoparticles in discriminating between the two proteins.

The median ΔF_n values measured after the detection did not show any dependency on n. Moreover, while the NIPs exhibited poor repeatability and high variability in their signals, the CS-sMI-NPs demonstrated more consistent and less variable responses. We detected a statistically relevant difference in the detection of BSA by the two systems (t-test, p-value < 0.05). No statistical differences were highlighted in the detection of STREP but a slight increase in absolute signal intensity was observed.

Normalized signals from detections against those measured in probe conjugation indicated that while the NIPs exhibited increased variability and poor reproducibility, the CS-sMI-NPs system maintained a stable nonspecific signal with BSA, which remained consistently lower than that obtained in STREP detection. Statistically significant differences were obtained only in the normalized signals obtained with CS-sMI-NPs (t-test, p-values < 0.05).

3.3 The case study

The characterization of the surface-imprinted nanoparticles toward tannins (CS-tMI-NPs) confirmed the promising performance of the tested system. Complexes between the template and the functionalized nanoparticles resulted 112 nm ± 31 nm, while the core/shell nanoparticles resulted 165 nm ± 31 nm. Both size measurements were in line with those obtained for the CS-sMI-NPs. Also the QCM-D results obtained from the new set of experiments for the adlayer (Fig. 8a) and probe (Fig. 8b) immobilization did not significantly vary compared to the previous set. Results from sample detection with CS-tMI-NPs-functionalized sensors (Fig. 8c) indicated higher binding for the template mixture (TVRG), lower binding for the mixture of different tannins (TG), and an intermediate behavior for the mixture containing proanthocyanidins and ellagitannins (TVRS). In contrast, NIPs (Fig. 8d) exhibited no differences between TVRG and TVRS detection and showed very limited adsorption of TG.

4 Discussion

Optimized core synthesis ensured high monomer conversion and consistent particle sizes, with TEOS concentration enabling tunable nanoparticle dimensions from 22 nm to 63 nm. The negative shift in ζ-potential with increasing TEOS concentration highlights the role of deprotonated silanol groups in surface charge modulation.[44]

Functionalization tests revealed that higher APTES-to-TMPMA ratios increased nanoparticle size, while elevated TMPMA concentrations inhibited surface functionalization. Formation of STREP/nanoparticle complexes was confirmed by size increases and UV-Vis analysis, indicating efficient protein binding driven by electrostatic interactions between negatively charged STREP at pH 7.4,[45] and the positively charged amine groups on the nanoparticles. The final bound STREP-to-nanoparticle ratio was 2.7 μg mg^{-1}. Molecular imprinting increased the specific surface area by 260–270%, providing an enhanced target accessibility. CS-sMI-NPs demonstrated higher STREP retention (34–37%) compared to non-imprinted controls (6–12%), as confirmed by Langmuir modeling, underscoring

the creation of specific binding sites despite relatively low affinity. The observed increase in specific surface area in the imprinted nanoparticles is not an independent variable, but a direct consequence of the molecular imprinting process itself. The formation of template-specific cavities at the nanoparticle surface leads to a structured, accessible polymer layer, which inherently increases the total surface area while enabling specific interactions. Therefore, the enhanced protein retention observed in CS-MI-NPs compared to NIP particles should not be attributed to surface area alone, but rather to the molecularly defined binding sites that simultaneously increase the surface and confer selectivity. This interpretation is further supported by the low and unspecific adsorption observed with BSA and the higher retention and affinity parameters measured for the target protein.

QCM-D results confirmed efficient adlayer formation and nanoparticle immobilization, with negative ΔF_n and ΔD_n values indicating a rigid, well-structured PEG layer stabilized by probe immobilization. During STREP detection, ΔF_n normalized over probe immobilization was approximately 11 times higher than biotinylated PEG-functionalized sensors.[43] CS-sMI-NPs showed higher specificity for STREP, while controls exhibited stronger nonspecific interactions with BSA, highlighting the selectivity introduced by molecular imprinting. CS-MI-NPs enabled STREP detection at 2.8 nM, comparable to other acoustic platforms such as Rayleigh Surface Acoustic Wave sensors with LoDs of 0.5 nM.[46] The selection of streptavidin and tannins as target analytes was intentional to evaluate the versatility and robustness of the CS-MI-NPs system across distinct chemical and structural classes. Streptavidin, a globular and well-characterized protein, represents a model analyte for biomedical applications, while tannins are highly heterogeneous polyphenolic compounds relevant to food and environmental analysis. Their inclusion enabled the assessment of the imprinting platform in terms of specificity, adaptability, and performance in both protein-based and non-proteinaceous systems, thus demonstrating the broad applicability of the developed sensing approach.

For tannins, CS-tMI-NPs selectively distinguished between proanthocyanidins, ellagic, and gallic tannins despite some nonspecific affinity for proanthocyanidins. Based on the estimated average molecular weights of proanthocyanidins (5000 Da) and tannins (1500 Da),[47] detection concentrations aligned with the capabilities of CS-tMI-NPs, which produced ΔF_n values comparable to biologically derived probes.[48,49] These results position CS-tMI-NPs as robust, synthetic alternatives for tannin detection in complex matrices.

5 Conclusion and perspectives

This research successfully developed and characterized core/shell nanoparticles (CS-MI-NPs) with potential for advanced biosensing applications. The systematic optimization of synthesis parameters and molecular imprinting demonstrated the versatility of these nanoparticles, achieving tailored properties with enhanced selectivity and performance. Future work will focus on refining functionalization techniques and expanding specificity by incorporating diverse molecular templates. Additionally, strategies such as surface modifications and inert blocking agents will be explored to minimize nonspecific binding. Testing in complex matrices, such as biological fluids or wine samples, will further assess their robustness under real-world conditions.

While foundational performance has been established, challenges such as LoD calculation, long-term stability and resilience in practical settings still need to be addressed. Detecting streptavidin in diagnostic assays or tannins in commercial wine will validate their utility against interference from complex components like sugars and alcohols. Despite these limitations, CS-MI-NPs combine enhanced specific surface areas with tailored binding properties, making them a significant advancement in biosensing technology. Their compatibility with acoustic detection platforms and high selectivity underscore their potential for applications in diagnostics, environmental monitoring, and other real-world settings.

By addressing current challenges and optimizing performance in heterogeneous environments, CS-MI-NPs could pave the way for next-generation biosensors with superior sensitivity, selectivity, and versatility across diverse fields.

Data availability

The data generated in this study, as well as the computational codes used for analysis, are not yet publicly available. However, a comprehensive dataset, including all relevant data and scripts, is currently being prepared and will be made publicly accessible in the near future.

Conflicts of interest

There are no conflicts of interest to declare.

Acknowledgements

Funded by the European Union – Next Generation EU, Mission 4 Component 2 Inv. 1.5 CUP: B83C22003930001 (Tuscany Health Ecosystem, Spoke 4: Nanotechnologies for Diagnosis and Therapy) and Regione Toscana, Bando Ricerca Salute 2018, "The Omics Sciences against Osteosarcoma – TOSCANO" CUP: B54I20002750002.

References

1 H. Zhang, *Adv. Mater.*, 2020, **32**, 1806328.
2 M. Gagliardi, *Adv. Ind. Eng. Polym. Res.*, 2023, **6**, 396–406.
3 J. Xu, H. Miao, J. Wang and G. Pan, *Small*, 2020, **16**, 1906644.
4 W. Zhang, Y. Zhang, R. Wang, P. Zhang, Y. Zhang, E. Randell and Q. Jia, *Anal. Chim. Acta*, 2022, **1234**, 340319.
5 K. Haupt and K. Mosbach, *Chem. Rev.*, 2000, **100**, 2495–2504.
6 S. Bahrani, E. S. Behbahani, M. Ghaedi, Y. A. Miandeh and A. Asfaram, *Microchem. J.*, 2024, 110888.
7 A. M. Mostafa, S. J. Barton, S. P. Wren and J. Barker, *TrAC, Trends Anal. Chem.*, 2021, **144**, 116431.

8 M. Drobysh, V. Ratautaite, E. Brazys, A. Ramanaviciene and A. Ramanavicius, *Biosens. Bioelectron.*, 2024, **251**, 116043.
9 Y. Li, L. Luo, Y. Kong, S. George, Y. Li, X. Guo and B. Li, *Adv. Funct. Mater.*, 2024, 2316865.
10 N. Nawaz, N. K. A. Bakar, H. N. M. E. Mahmud and N. S. Jamaludin, *Anal. Biochem.*, 2021, **630**, 114328.
11 Y. Hua, Y. Ahmadi and K. H. Kim, *Environ. Pollut.*, 2022, **311**, 119931.
12 T. Wasilewski, S. Orbay, N. F. Brito, K. Sikora, A. C. A. Melo, M. E. Melendez and J. Gębicki, *TrAC, Trends Anal. Chem.*, 2024, 117783.
13 B. Tse Sum Bui, A. Mier and K. Haupt, *Small*, 2023, **19**, 2206453.
14 M. Mabrouk, S. F. Hammad, A. A. Abdella and F. R. Mansour, *Microchem. J.*, 2023, 109152.
15 H. R. Culver and N. A. Peppas, *Chem. Mater.*, 2017, **29**, 5753–5761.
16 C. J. Tan and Y. W. Tong, *Anal. Bioanal. Chem.*, 2007, **389**, 369–376.
17 C. Dong, H. Shi, Y. Han, Y. Yang, R. Wang and J. Men, *Eur. Polym. J.*, 2021, **145**, 110231.
18 M. Pan, L. Hong, X. Xie, K. Liu, J. Yang and S. Wang, *Macromol. Chem. Phys.*, 2021, **222**, 2000222.
19 T. Matsunaga, T. Hishiya and T. Takeuchi, *Anal. Lett.*, 2007, **40**, 2633–2640.
20 A. Mueller, *Molecules*, 2021, **26**, 5139.
21 G. Wulff and J. Liu, *Acc. Chem. Res.*, 2012, **45**, 239–247.
22 N. V. Phan, H. F. Sussitz and P. A. Lieberzeit, *Biosensors*, 2014, **4**, 161–171.
23 A. N. Hasanah, N. Safitri, A. Zulfa, N. Neli and D. Rahayu, *Molecules*, 2021, **26**, 5612.
24 M. Niu, C. Pham-Huy and H. He, *Microchim. Acta*, 2016, **183**, 2677–2695.
25 M. Gagliardi, M. Agostini, F. Lunardelli, L. Lamanna, A. Miranda, A. Bazzichi and M. Cecchini, *Sens. Actuators, B*, 2023, **379**, 133299.
26 M. Gagliardi, M. Agostini, F. Lunardelli, A. Miranda, A. G. Luminare, F. Cervelli and M. Cecchini, *Biosensors*, 2022, **12**, 1010.
27 M. Gagliardi, L. Colagiorgio and M. Cecchini, *Biosensors*, 2023, **13**, 607.
28 M. Agostini, F. Lunardelli, M. Gagliardi, A. Miranda, L. Lamanna, A. G. Luminare and M. Cecchini, *Adv. Funct. Mater.*, 2022, **32**, 2201958.
29 A. Yarman, S. Kurbanoglu, I. Zebger and F. W. Scheller, *Sens. Actuators, B*, 2021, **330**, 129369.
30 S. Akgönüllü, S. Kılıç, C. Esen and A. Denizli, *Polymers*, 2023, **15**, 629.
31 I. LariMojarad, M. Mousavi, M. M. Moeini Manesh, M. Bouloorchi Tabalvandani, M. Badieirostami and M. A. Janjua, *ACS Omega*, 2024, **9**, 16026–16034.
32 V. Kumar and W. Kutner, *Chem. Eng. J.*, 2024, 155828.
33 J. Shang and X. Gao, *Chem. Soc. Rev.*, 2014, **43**, 7267–7278.
34 A. A. Vasilyeva, R. A. Buribaev, M. V. Gorbunova, V. V. Apyari, I. I. Torocheshnikova and S. G. Dmitrienko, *TrAC, Trends Anal. Chem.*, 2024, 117538.
35 M. Włoch and J. Datta, *Compr. Anal. Chem.*, 2019, **86**, 17–40.
36 J. O. Amode, J. H. Santos, Z. Md. Alam, A. H. Mirza and C. C. Mei, *Int. J. Ind. Chem.*, 2016, **7**, 333–345.
37 A. Acharya, G. Jeppu, C. Raju, B. Prabhu and A. Girish, *Langmuir*, 2023, **39**, 17862–17878.
38 A. K. Dutta and G. Belfort, *Langmuir*, 2007, **23**, 3088–3094.
39 G. Sauerbrey, *Z. Phys.*, 1959, **155**, 206–212.
40 I. Reviakine, D. Johannsmann and R. P. Richter, *Langmuir*, 2011, **27**, 8838–8848.
41 B. D. Vogt, E. K. Lin, W. L. Wu and C. C. White, *J. Phys. Chem. B*, 2004, **108**, 12685–12690.
42 S. Mushtaq, M. A. Abbas, H. Nasir, A. Mahmood, M. Iqbal, H. A. Janjua and N. M. Ahmad, *Sci. Rep.*, 2023, **13**, 4572.
43 S. Dutta, M. Gagliardi, L. Bellucci, M. Agostini, S. Corni, M. Cecchini and G. Brancolini, *Front. Mol. Biosci.*, 2022, **9**, 1006525.
44 B. M. Lowe, C. K. Skylaris and N. G. Green, *J. Colloid Interface Sci.*, 2015, **451**, 231–244.
45 A. A. Choi and K. Xu, *J. Am. Chem. Soc.*, 2024, **146**, 10973–10978.
46 M. Agostini, G. Greco and M. Cecchini, *Sens. Actuators, B*, 2018, **254**, 1–7.
47 J. M. McRae, N. Kirby, H. D. Mertens, S. Kassara and P. A. Smith, *J. Agric. Food Chem.*, 2014, **62**, 7216–7224.
48 M. Gagliardi, G. Tori, M. Agostini, F. Lunardelli, F. Mencarelli, C. Sanmartin and M. Cecchini, *Nanomaterials*, 2022, **12**, 166.
49 M. Gagliardi, G. Tori, C. Sanmartin and M. Cecchini, *J. Sci. Food Agric.*, 2025, **105**, 1476–1483.